

# A Slice-Low-Rank Plus Sparse (slice-L + S) Reconstruction Method for k-t Undersampled Multiband First-Pass Myocardial Perfusion MRI

Changyu Sun<sup>1,2,3</sup>  | Austin Robinson<sup>4</sup> | Yu Wang<sup>1</sup> | Kenneth C. Bilchick<sup>4</sup> | Christopher M. Kramer<sup>4,5</sup> | Daniel Weller<sup>1,6,5</sup>  | Michael Salerno<sup>1,4,5</sup> | Frederick H. Epstein<sup>1,5</sup>

<sup>1</sup>Department of Biomedical Engineering, University of Virginia, Charlottesville, Virginia

<sup>2</sup>Department of Biomedical, Biological and Chemical Engineering, University of Missouri, Columbia, Missouri

<sup>3</sup>Department of Radiology, University of Missouri, Columbia, Missouri

<sup>4</sup>Department of Medicine, University of Virginia Health System, Charlottesville, Virginia

<sup>5</sup>Department of Radiology, University of Virginia Health System, Charlottesville, Virginia

<sup>6</sup>Department of Electrical and Computer Engineering, University of Virginia, Charlottesville, Virginia

## Correspondence

Frederick H. Epstein, Departments of Biomedical Engineering and Radiology, University of Virginia, Charlottesville, VA 22908.

Email: [fredepstein@virginia.edu](mailto:fredepstein@virginia.edu)

## Funding information

National Heart, Lung, and Blood Institute, Grant/Award Number: R01 HL147104; University of Virginia Coulter Translational Research Partnership

**Purpose:** The synergistic use of k-t undersampling and multiband (MB) imaging has the potential to provide extended slice coverage and high spatial resolution for first-pass perfusion MRI. The low-rank plus sparse (L + S) model has shown excellent performance for accelerating single-band (SB) perfusion MRI.

**Methods:** A MB data consistency method employing ESPIRiT maps and through-plane coil information was developed. This data consistency method was combined with the temporal L + S constraint to form the slice-L + S method. Slice-L + S was compared to SB L + S and the sequential operations of split slice-GRAPPA and SB L + S (seq-SG-L + S) using synthetic data formed from multislice SB images. Prospectively k-t undersampled MB data were also acquired and reconstructed using seq-SG-L + S and slice-L + S.

**Results:** Using synthetic data with total acceleration rates of 6–12, slice-L + S outperformed SB L + S and seq-SG-L + S (N = 7 subjects) with respect to normalized RMSE and the structural similarity index ( $P < 0.05$  for both). For the specific case with MB factor = 3 and rate 3 undersampling, or for SB imaging with rate 9 undersampling (N = 7 subjects), the normalized RMSE values were  $0.037 \pm 0.007$ ,  $0.042 \pm 0.005$ , and  $0.031 \pm 0.004$ ; and the structural similarity index values were  $0.88 \pm 0.03$ ,  $0.85 \pm 0.03$ , and  $0.89 \pm 0.02$  for SB L + S, seq-SG-L + S, and slice-L + S, respectively ( $P < 0.05$  for both). For prospectively undersampled MB data, slice-L + S provided better image quality than seq-SG-L + S for rate 6 (N = 7) and rate 9 acceleration (N = 7) as scored by blinded experts.

**Conclusion:** Slice-L + S outperformed SB-L + S and seq-SG-L + S and provides 9 slice coverage of the left ventricle with a spatial resolution of  $1.5 \text{ mm} \times 1.5 \text{ mm}$  with good image quality.

## KEYWORDS

first-pass myocardial perfusion MRI, multiband, parallel imaging, simultaneous multislice, slice-Low rank plus sparse, compressed sensing

## 1 | INTRODUCTION

First-pass myocardial perfusion MRI plays an important role in the clinical assessment of ischemic heart disease.<sup>1</sup> Although the method is very useful, current clinical protocols generally acquire 3 slices with 2–3 mm in-plane spatial resolution,<sup>2</sup> and greater slice coverage and higher spatial resolution could improve clinical performance.<sup>3,4</sup> However, achieving greater slice coverage and higher spatial resolution is technically challenging because of the requirements to provide high temporal resolution and high SNR,<sup>2</sup> making the use of optimized acceleration methods essential. Both k-t undersampling methods<sup>5–7</sup> and simultaneous multislice (or multiband (MB)) methods can be applied to first-pass MRI, and their synergistic use for this application has high potential.<sup>8–12</sup>

The use of k-t undersampling for single-band (SB) first-pass MRI has been studied extensively, including with parallel imaging,<sup>13,14</sup> compressed sensing,<sup>5</sup> parallel imaging with compressed sensing,<sup>6</sup> low-rank methods,<sup>15</sup> and sparse and low-rank methods.<sup>7,16</sup> An important finding was that of joint sparsity,<sup>6,7</sup> where it was shown that compressed sensing regularization methods such as low-rank plus sparse (L + S)<sup>7</sup> are more effective and efficient when applied to coil-combined data because correlations between coils are simultaneously exploited with compressed sensing regularizations. In addition, the L + S matrix decomposition model outperformed k-t SPARSE for accelerated first-pass MRI by exploiting the ability of low rank to approximate the background signal and the ability of compressed sensing to approximate the dynamic signal.<sup>7</sup>

Whereas k-t undersampled methods that utilize parallel imaging make use of in-plane coil sensitivities, MB imaging is an alternative method to acquire more slices per unit time, utilizing through-plane coil information to separate data acquired simultaneously from multiple slices.<sup>17–20</sup> For MB imaging without k-t undersampling, the SNR is not reduced by  $\sqrt{R}$ , where R is the in-plane acceleration rate. Furthermore, MB imaging with controlled aliasing in parallel imaging (CAIPIRINHA)<sup>21</sup> has a favorable geometry factor, providing further SNR advantages. Slice separation of MB data is performed effectively using the split slice-GRAPPA (SG) method,<sup>19</sup> which utilizes a through-plane GRAPPA kernel calibrated to reduce slice separation artifacts. For k-t undersampled MB first-pass MRI, the sequential operations of compressed sensing and slice separation have been used<sup>8</sup>; however, sequential operations do not globally minimize the aggregate error from multiple sources. Iterative MB CG-SENSE simultaneously reduces in-plane and through-plane artifacts<sup>22</sup>; however, it does not use through-plane coil information to its fullest potential, resulting in residual

artifacts.<sup>18,22</sup> Recently, slice-SPIRiT was introduced to iteratively utilize through-plane coil information for slice separation in a MB data consistency term while simultaneously enforcing in-plane coil calibration consistency.<sup>23</sup> The slice-SPIRiT study showed the advantage of utilizing in-plane SPIRiT kernels and slice separation using split slice-GRAPPA applied coil by coil in an integrated iterative model for MB reconstruction, and it showed the potential to add regularization terms such as temporal sparse or low rank constraints. However, slice-SPIRiT did not provide joint sparsity of slice-separated data.

To develop an improved reconstruction method for k-t undersampled MB first-pass imaging, we propose a method that uses slice-separating kernels followed by coil combination to compute coil-combined slice-separated gradients for the data consistency term that enable the use of L + S regularization applied to slice-separated coil-combined images (slice-separated joint sparsity). We also address challenges related to solving the slice-L + S minimization problem, which includes  $l_2$ ,  $l_1$ , and nuclear norm terms. Slice-L + S (with MB = 3 and R = 2–4) is evaluated using synthetic undersampled MB first-pass images generated from SB images of human subjects. Using synthetic data, slice-L + S is compared to undersampled SB first-pass imaging with a SB L + S reconstruction and to MB reconstruction using the sequential operations of slice separation followed by SB L + S (seq-SG-L + S), all with the same total acceleration rates of 6–12. Slice-L + S is also compared to seq-SG-L + S using prospectively acquired undersampled MB first-pass data from human subjects with MB = 3 and R = 2 and 3. An overview of the methods investigated in this study is provided in Figure 1.

## 2 | THEORY

To integrate the use of in-plane coil sensitivities, through-plane coil information, temporal L + S constraint, and simultaneous reduction of artifacts due to k-t undersampling and slice separation, we propose a slice-L + S method to provide slice-separated joint sparsity of coils and L + S of concatenated coil-combined slice-separated images. Slice-L + S includes a new MB data consistency method to jointly enforce data consistency of all separated slices. Because we will compare slice-L + S to seq-SG-L + S (and to SB L + S), we will first describe the implementation of seq-SG-L + S (SB L + S has previously been described<sup>7</sup>).

### 2.1 | Sequential operations method (seq-SG-L + S)

The seq-SG-L + S reconstruction model (Figure 1) first applies split slice-GRAPPA<sup>19</sup> for slice separation and

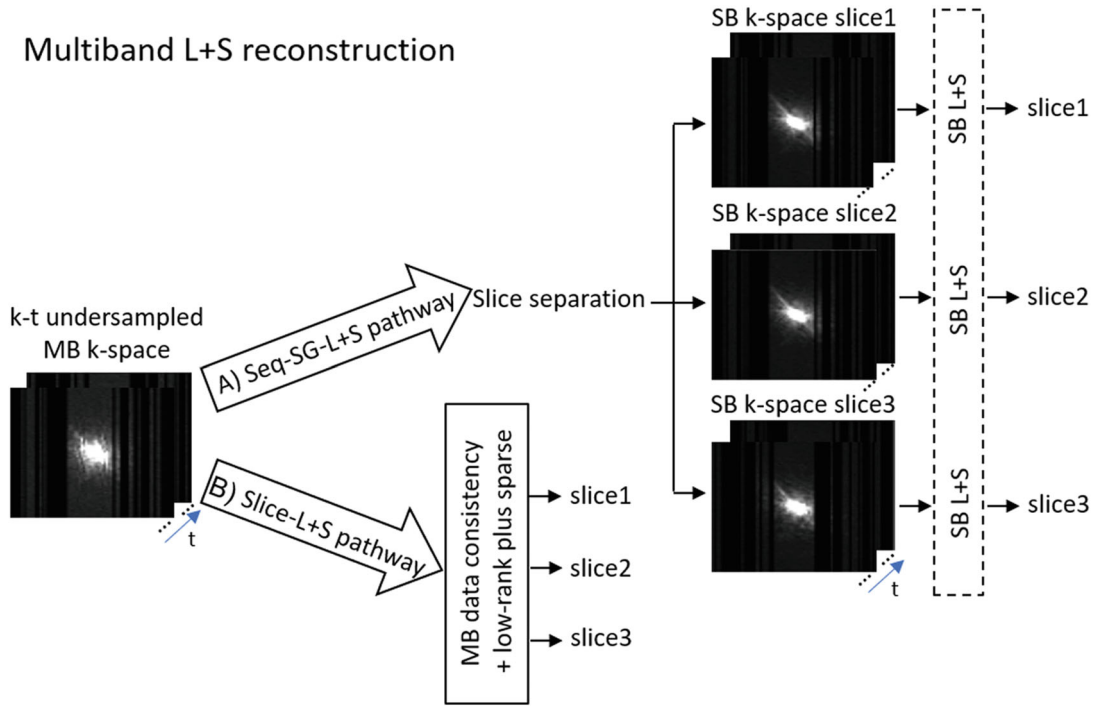


**FIGURE 1** Reconstruction schemes for k-t undersampled MB data including (A) the sequential operations method of split slice-GRAPPA followed by single-band L + S (seq-SG-L + S), and (B) the integrated use of MB data consistency and L + S of multiple slices (slice-L + S). (A) For seq-SG-L + S, a split slice-GRAPPA kernel is applied to separate k-t undersampled MB  $k$ -space data, and then the separated data are input into SB L + S. (B) The slice-L + S method employs an integrated approach that simultaneously optimizes MB data consistency and jointly enforces the L + S constraint of multiple separated slices. L + S, low-rank plus sparse; MB, multiband; seq-SB L + S, sequential operations of split slice-GRAPPA and SB L + S.

then applies SB L + S.<sup>7</sup> The use of split slice-GRAPPA is expressed as:

$$\mathbf{y}_z = \mathbf{P}_z^* \mathbf{K}_z \mathbf{y}_{MB}, \quad (1)$$

where  $\mathbf{y}_{MB}$  is the MB multicoil  $k$ -space data;  $\mathbf{P}_z^*$  is the CAIPRINHA phase demodulation matrix;  $\mathbf{K}_z$  is the split slice-GRAPPA kernel; and  $\mathbf{y}_z$  is the separated  $k$ -space data corresponding to slice  $z$  ( $z = 1, 2, \dots, N_s$ ) where  $N_s$  is the number of MB slices. Using  $\mathbf{y}_z$  from Equation 1 in the data consistency term, the standard SB L + S reconstruction model for slice  $z$  is described in Equation 2 as:

$$\underset{\mathbf{L}_z, \mathbf{S}_z}{\operatorname{argmin}} \left\| \mathbf{A}_z (\mathbf{L}_z + \mathbf{S}_z) - \mathbf{y}_z \right\|^2 + \lambda_L \|\mathbf{L}_z\|_* + \lambda_S \|T(\mathbf{S}_z)\|_1, \quad (2)$$

where  $\mathbf{L}_z$  and  $\mathbf{S}_z$ , respectively, represent the low-rank and the sparse components of the  $z^{\text{th}}$  slice (the reconstructed image =  $\mathbf{L}_z + \mathbf{S}_z$ ); the operator  $\mathbf{A}_z = \mathbf{f}_t \mathbf{E}_z$ ; and  $\mathbf{A}_z^* = \mathbf{E}_z^* \mathbf{f}_t^{-1}$  is the Hermitian adjoint of  $\mathbf{A}_z$ ;  $\mathbf{f}_t$  is the fast Fourier transform (FFT);  $\mathbf{f}_t^{-1}$  is the inverse fast Fourier transform (IFFT) and application of the sampling mask of the  $t^{\text{th}}$  measurement;  $\mathbf{E}_z$  is the ESPIRiT map for the  $z^{\text{th}}$  slice;  $\lambda_L$  is the weight for the low-rank nuclear norm constraint;  $\lambda_S$  is the weight for the temporal frequency  $l_1$ -norm constraint; and  $T$  is the temporal FFT operator. A simplified notation

is being used without showing the temporal dimension in Equations 1–2 (e.g.,  $\mathbf{L}_z$  refers to  $\mathbf{L}_z[x, y, t]$ ;  $\mathbf{S}_z$  refers to  $\mathbf{S}_z[x, y, t]$ ; and  $\mathbf{y}_z$  refers to  $\mathbf{y}_z[x, y, \text{coil}, t]$ ). Here, if  $\mathbf{x}$  is an image, then  $\|\mathbf{x}\|_*$  is the nuclear norm, which is defined as the sum of singular values of the matrix  $\mathbf{x}$ . The  $l_1$  norm is defined as the sum of absolute values given by  $\|\mathbf{x}\|_1 = \sum_i |x_i|$  of the matrix  $\mathbf{x}$ . The  $l_2$  norm is defined as the sum of values given by  $\|\mathbf{x}\|_2 = (\sum_i |x_i|^2)^{1/2}$  of the matrix  $\mathbf{x}$ .

## 2.2 | Slice-L + S

Here we introduce the slice-L + S reconstruction method that enforces consistency with the acquired MB data and also enforces temporal low-rank plus sparse constraints applied to multiple slices. The proposed slice-L + S reconstruction model (Figure 2) is expressed in Equation 3 as:

$$\underset{\mathbf{L}, \mathbf{S}}{\operatorname{argmin}} \left\| \mathbf{H} \begin{pmatrix} \mathbf{L}_1 + \mathbf{S}_1 \\ \mathbf{L}_2 + \mathbf{S}_2 \\ \dots \\ \mathbf{L}_{N_s} + \mathbf{S}_{N_s} \end{pmatrix} - \mathbf{y}_{MB} \right\|^2 + \lambda_L \left\| \begin{pmatrix} \mathbf{L}_1 \\ \mathbf{L}_2 \\ \dots \\ \mathbf{L}_{N_s} \end{pmatrix} \right\|_* + \lambda_S \left\| T \begin{pmatrix} \mathbf{S}_1 \\ \mathbf{S}_2 \\ \dots \\ \mathbf{S}_{N_s} \end{pmatrix} \right\|_1, \quad (3)$$

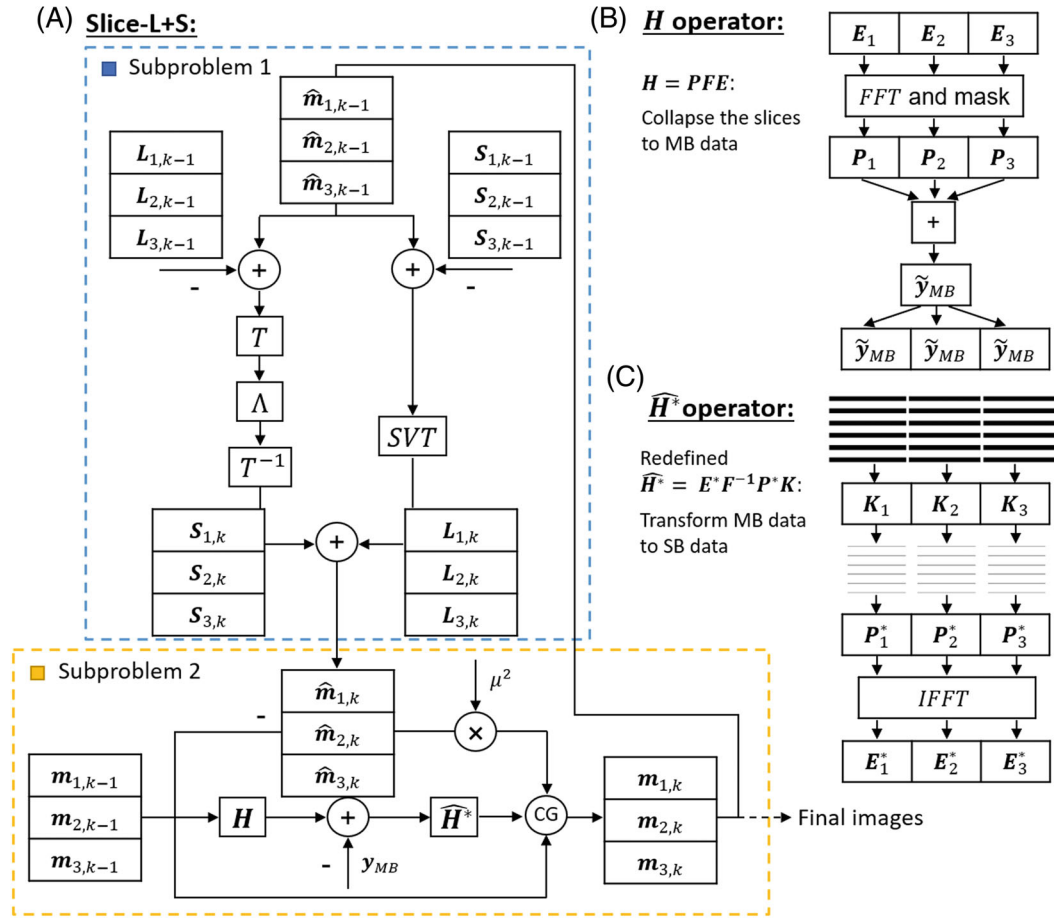


**FIGURE 2** Schematic of the solution of the slice-L + S method of Equations 3–6, alternating between the conjugate gradient solution of the MB data consistency subproblem and the soft thresholding solution of the L + S subproblem using variable splitting. (A) Images of all slices are initialized to 0. Subproblem 1 applies soft thresholding to solve the L + S optimization of coil-combined images of readout concatenated separated slices. Specifically, singular value soft thresholding (second term, Equation 3), and soft thresholding of temporal sparsity using the temporal FFT (third term, Equation 3) are used. Subproblem 2 employs the conjugate gradient method to solve the MB data consistency term (first term, Equation 3). Subproblem 2 pertains to consistency with the  $k$ - $t$  undersampled MB data and utilizes the slice-collapsing ( $H$ ) and slice-separating ( $\widehat{H}^*$ ) operations. In (B), the  $H$  operator of Equation 3 is depicted, showing multiplication by ESPIRiT maps, FFT, and application of undersampling masks for each temporal frame, phase modulation, summation operation, and repeat of CAIPiRiNHA-modulated MB data for each slice. In (C), the  $\widehat{H}^*$  operator of Equation 3 is depicted, including application of the slice-separating  $K$  kernels, phase demodulation, the IFFT transform and coil combination using ESPIRiT maps. Bold  $k$ -space lines indicate MB  $k$ -space data. Non-bold  $k$ -space lines indicate SB  $k$ -space data. CAIPiRiNHA, controlled aliasing in parallel imaging; FFT, fast Fourier transform;  $H$ , slice-collapsing;  $\widehat{H}^*$ , slice-separating; IFFT, inverse fast Fourier transform; SB, single-band.

where the operator  $H$  (as shown in Figure 2B) is defined as  $H = (P_1 f_1 E_1, P_2 f_2 E_2, \dots, P_{N_s} f_{N_s} E_{N_s}) = PFE$ ;  $P_z$  is the CAIPiRiNHA phase modulation matrix for the  $z^{\text{th}}$  slice;  $P = (P_1, P_2, \dots, P_{N_s})$ ;  $F = \begin{pmatrix} f_1 & \dots & 0 \\ \vdots & \ddots & \vdots \\ 0 & \dots & f_{N_s} \end{pmatrix}$ ; and

$$E = \begin{pmatrix} E_1 & \dots & 0 \\ \vdots & \ddots & \vdots \\ 0 & \dots & E_{N_s} \end{pmatrix}. \text{ In Equation 3, } L = \begin{pmatrix} L_1 \\ L_2 \\ \dots \\ L_{N_s} \end{pmatrix} \text{ and}$$

$S = \begin{pmatrix} S_1 \\ S_2 \\ \dots \\ S_{N_s} \end{pmatrix}$  represent the concatenated  $N_s$  coil-combined

low-rank and sparse components of the images undergoing reconstruction. A simplified notation is being used neglecting the temporal dimension (e.g.,  $L$  refers to  $L[x, y, z, t]$ ;  $S$  refers to  $S[x, y, z, t]$ ; and  $y_{MB}$  refers to  $y_{MB}[x, y, \text{coil}, t]$ ). Next, we define the conjugate of  $H$  as  $H^*$ , and we further define an approximation of  $H^*$  as  $\widehat{H}^* = E^* F^{-1} P^* K$ , providing the use of through-plane coil information and in-plane slice-by-slice ESPIRiT maps for slice separation (Figure 2C), similar to the slice separation

method employed for slice-SPIRiT.<sup>23</sup> Here  $P^* = \begin{pmatrix} P_1^* \\ P_2^* \\ \dots \\ P_{N_s}^* \end{pmatrix}$  is

the phase-demodulation operator for all slices;  $F^{-1}$  is the IFFT for all slices; and  $\mathbf{K} = \begin{pmatrix} \mathbf{K}_1 & \cdots & 0 \\ \vdots & \ddots & \vdots \\ 0 & \cdots & \mathbf{K}_{N_s} \end{pmatrix}$  performs a convolution using slice-separating split slice-GRAPPA kernels for all slices. It is through the use of  $\mathbf{E}$  in  $\mathbf{H}$  as well as  $\mathbf{E}^*$  and  $\mathbf{K}$  in  $\widehat{\mathbf{H}}^*$  that, in this new MB data consistency term, slice-L + S utilizes both in-plane coil sensitivity and through-plane coil information (Figure 2C).

Notably, the present MB data consistency method is designed to provide a coil-combined slice-by-slice gradient using both split slice-GRAPPA<sup>19,23</sup> and ESPIRiT<sup>24,25</sup> for efficiently reducing artifacts due to slice separation and k-t undersampling. In addition, this method applies the temporal L + S matrix decomposition to multiple images that undergo slice separation.

To solve this optimization problem, variable splitting<sup>26</sup> is employed as shown in Figure 2 and expressed as:

$$\begin{aligned} \underset{\mathbf{m}, \widehat{\mathbf{m}}}{\operatorname{argmin}} & \left\| \mathbf{H} \begin{pmatrix} \mathbf{m}_1 \\ \mathbf{m}_2 \\ \vdots \\ \mathbf{m}_{N_s} \end{pmatrix} - \mathbf{y}_{MB} \right\|^2 + \lambda_L \left\| \begin{pmatrix} \mathbf{L}_1 \\ \mathbf{L}_2 \\ \vdots \\ \mathbf{L}_{N_s} \end{pmatrix} \right\|_* \\ & + \lambda_S \left\| T \begin{pmatrix} \mathbf{S}_1 \\ \mathbf{S}_2 \\ \vdots \\ \mathbf{S}_{N_s} \end{pmatrix} \right\|_1 + \mu^2 \|\mathbf{m} - \widehat{\mathbf{m}}\|^2, \end{aligned} \quad (4)$$

where  $\widehat{\mathbf{m}} = \mathbf{L} + \mathbf{S}$  is an auxiliary variable. Equation 4 is decomposed into 2 subproblems. The  $\mathbf{m}$  optimization subproblem is written as

$$\underset{\mathbf{m}}{\operatorname{argmin}} \|\mathbf{H}\mathbf{m} - \mathbf{y}_{MB}\|^2 + \mu^2 \|\mathbf{m} - \widehat{\mathbf{m}}\|^2, \quad (5)$$

and is solved using the conjugate gradient algorithm. The  $\widehat{\mathbf{m}} = \mathbf{L} + \mathbf{S}$  subproblem is written as

$$\underset{\mathbf{L}, \mathbf{S}}{\operatorname{argmin}} \lambda_L \|\mathbf{L}\|_* + \lambda_S \|\mathbf{S}\|_1 + \|\mathbf{m} - \widehat{\mathbf{m}}\|^2, \quad (6)$$

and is solved using iterative soft thresholding. In Equation 6,  $\mu^2$  trades off the iterative speed between splitting iterations and conjugate gradient iterations.

### 3 | METHODS

Slice-L + S was evaluated for first-pass perfusion MRI. MRI was performed using a 1.5 Tesla system (MAGNETOM Aera, Healthcare, Erlangen, Germany) with chest and spine phased-array receiver coils (20–34 channels).

SB datasets, either with full sampling or using rate 2 undersampling, were acquired from patients to facilitate the generation of synthesized undersampled images. Synthetic MB data were used to determine the parameters in the reconstructions and to compare the proposed slice-L + S method to seq-SG-L + S and to SB L + S using the same total acceleration rates. Lastly, prospectively acquired k-t-undersampled MB imaging of patients was performed, and the slice-L + S method was compared by expert readers to seq-SG-L + S. The comparison of slice-L + S and SB L + S was made in order to evaluate a SB k-t undersampled acquisition and L + S reconstruction versus a MB k-t undersampled acquisition and slice-L + S reconstruction. The comparison of slice-L + S and sequential operations was made in order to evaluate the use of integrated operations with L + S of multiple slices versus sequential operations with SB L + S, keeping a consistent L + S regularization.

#### 3.1 | Pulse sequence

A saturation-recovery gradient-echo sequence was modified to use either SB or MB excitation with CAIPIRINHA phase modulation and Poisson-disc k-t undersampling. To acquire SB data to be used to form synthetic MB images, we either acquired fully sampled data or we acquired rate 2 undersampled data (even lines in even heartbeats and odd lines in odd heartbeats). A standard sinc pulse was used for SB RF excitation, and simple MB excitation pulses were implemented by summing 3 sinc pulses with appropriate phase modulation, as described.<sup>27</sup> For MB acquisitions, SB kernel calibration data were acquired in the first heartbeat. Twenty-four phase-encoding lines at the center of  $k$ -space for each slice were acquired, and calibration data for multiple slices were acquired consecutively.<sup>6,28</sup>

#### 3.2 | Image reconstruction

All image reconstruction was performed offline on a desktop computer using MatLab 2019a (MathWorks, Inc., Natick, MA). Split slice-GRAPPA kernels were fitted as described.<sup>19</sup> In-plane ESPIRiT maps were calculated based on the ESPIRiT algorithm.<sup>29</sup> The SB L + S method was solved using iterative soft thresholding as described<sup>7</sup> and was utilized for seq-SG-L + S. The slice-L + S reconstruction was split into MB data consistency and L + S parts: the first part was solved by conjugate gradient using LSQR,<sup>29</sup> and the second part was solved using iterative soft thresholding.<sup>7</sup> The 2 parts were connected using variable splitting.<sup>26,29</sup>

For rate 2 undersampled data, even  $k$ -space lines in even heartbeats and odd lines in odd heartbeats were firstly reconstructed by merging data from 2 successive heartbeats to generate SB reference data. The IFFT reconstructions of SB data were used as the reference standard to quantify the errors of various reconstruction methods. Using these reference images, the normalized RMSE (nRMSE)<sup>30</sup> and the structural similarity (SSIM)<sup>31</sup> were computed for each reconstruction method. The nRMSE was computed as:

$$nRMSE = \frac{1}{\max(m) - \min(m)} \sqrt{\frac{1}{N} \sum_{i=0}^{N-1} (m(i) - \tilde{m}(i))^2}, \quad (7)$$

where  $\tilde{m}$  is the concatenated SB images matched with the MB reconstructed images;  $m$  is the concatenated reconstructed images of simultaneously acquired slices; and  $N$  is the total number of pixels. The SSIM was computed as:

$$SSIM = \frac{(2\mu_m\mu_{\tilde{m}} + c_1)(2\sigma_{m\tilde{m}} + c_2)}{(\mu_m^2 + \mu_{\tilde{m}}^2 + c_1)(\sigma_m^2 + \sigma_{\tilde{m}}^2 + c_2)}, \quad (8)$$

where  $\mu_m$  and  $\sigma_m$  are the average and variance of  $m$ ;  $\sigma_{m\tilde{m}}$  is the covariance of  $m$  and  $\tilde{m}$ ; and  $c_1$  and  $c_2$  are variables that stabilize the division with a weak denominator, chosen as described in Ref.<sup>31</sup>

The split slice-GRAPPA kernel size was of the size  $5 \times 5$ , as used in the original slice-GRAPPA work,<sup>18</sup> and ESPIRiT maps used a kernel size of  $6 \times 6$ .<sup>29</sup> For SB L + S, images were initialized using coil combination after IFFT of  $k$ -t undersampled SB data.<sup>7</sup> For seq-SG-L + S, images were initialized using slice separation by split slice-GRAPPA, IFFT, and coil combination applied to  $k$ -t undersampled MB data. The weighting parameters of  $\lambda_L = 0.014$  and  $\lambda_S = 0.018 \times M_0$  for SB L + S and  $\lambda_L = 0.018$  and  $\lambda_S = 0.026 \times M_0$  for seq-SG-L + S were found to minimize the nRMSE relative to SB reference images, as shown in Supporting Information Figures S7 and S8, where  $M_0$  is the maximum magnitude of the initialized images.

For the slice-L + S method, images were initialized to 0 because split slice-GRAPPA is used in MB data consistency term of Equation 3. The slice-L + S weighting parameters of  $\lambda_L$  and  $\lambda_S$  were determined by comparing reconstructed images of synthetic MB data to the SB reference images over a range of values. Regularization parameter values of 0.01 for  $\lambda_L$  and  $0.01 \times M_0$  for  $\lambda_S$  were found to minimize the nRMSE relative to SB reference images, as shown in the Supporting Information Figure S6A. The parameter  $\mu^2$  was selected as 0.4, which is the same value used in  $l_1$ -ESPIRiT.<sup>29</sup> Although the parameters for the reconstructions were mainly found by minimizing nRMSE, we also considered the SSIM values

and the visualized image quality to find the overall best parameters.

To reduce the reconstruction time, coil compression was performed at 5% tolerance for the MB datasets before application of the iterative reconstruction methods using a method similar to SB coil compression.<sup>32</sup> The number of virtual coils was about half of the number of original coils. For SB L + S and seq-SG-L + S, we used the same stopping criterion as in Ref.<sup>7</sup> For slice-L + S, the iterative procedure was terminated when the change in the data consistency term was less than  $10^{-5}$  or a preset number of 25 iterations was reached<sup>22</sup> as justified in Supporting Information Figure S6B.

### 3.3 | Comparison of slice-L + S with SB L + S and seq-SG-L + S using synthetic undersampled MB data

SB first-pass images were acquired at rest from 7 patients to generate synthetic data with reference standard images. All patients provided informed consent, and all studies were performed in accordance with protocols approved by our institutional review board. Patient information is provided in Supporting Information Appendix S2. First-pass MRI utilized prospective electrocardiogram triggering, patients were instructed to breathhold as long as possible and then breathe shallowly when they could no longer breathhold, and 0.075 mmol/kg of gadolinium-based contrast agent (Dotarem, Guerbet, Paris, France) was injected intravenously at a rate of 4 mL/s, followed by 25 mL of saline flush at 4 mL/s. Three short-axis slices were acquired at basal, midventricular, and apical locations using SB saturation-recovery gradient-echo acquisitions. For fully sampled ( $N = 3$  patients) and rate-2 undersampled merged SB datasets ( $N = 4$ ), common sequence parameters included 3 slices per heartbeat, saturation-recovery delay time = 20 ms, repetitions = 40, flip angle =  $12^\circ$ – $15^\circ$ , slice thickness = 8–10 mm, and interslice gap of 12.5–16 mm. For fully sampled datasets, FOV =  $320 \times 238$ – $307$  mm<sup>2</sup>, TR = 2.42 ms, TE = 1.23 ms, spatial resolution =  $3.3$  mm  $\times$   $3.3$  mm, bandwidth = 1002 Hz/pixel, and temporal resolution = 172.8–222.6 ms, respectively, for the 3 patients, corresponding to phase FOV values of 74.4%–95.8%. For rate 2 merged datasets, FOV =  $360$ – $380 \times 270$ – $288$  mm<sup>2</sup>, TR = 1.94 ms, TE = 1 ms, spatial resolution =  $2.25$  mm  $\times$   $2.25$  mm, bandwidth = 650 Hz/pixel and temporal resolution = 169.4–180.7 ms, respectively for the 4 patients, corresponding to phase FOV values of 75%–80%.

These SB datasets were used to synthesize  $k$ -t undersampled MB images with MB = 3 and R = 2–4

by applying CAIPIRINHA phase modulation, summing them, and applying the Poisson-disc k-t undersampling mask. SB k-t undersampled data with the same total accelerations of  $R = 6-12$  were simulated by applying the Poisson-disc k-t undersampling mask to SB k-space. The simulated undersampled SB datasets were reconstructed using SB L+S, and the synthesized undersampled MB datasets were reconstructed using seq-SG-L+S and slice-L+S. To quantitatively compare these methods, nRMSE and SSIM were computed using fully sampled or rate 2 merged SB images as the reference.

Normalized RMSE and SSIM were assessed using 2-way analysis of variance with a statistically significant difference defined as  $P < 0.05$ . Pairwise comparisons were evaluated using the Bonferroni post hoc test with adjusted  $P$  values, where the 2 factors were measurements and reconstruction methods, and replications occurred over subjects.

### 3.4 | Comparison of slice-L + S with seq-SG-L + S for the reconstruction of prospectively acquired k-t undersampled MB first-pass data

To evaluate reconstruction methods for prospectively acquired k-t undersampled MB imaging, 7 patients were scanned using  $MB = 3$  and  $R = 2$ , and 7 patients were scanned using  $MB = 3$  and  $R = 3$ . Scan parameters were 9 slices per heartbeat (6 slices per heartbeat in 1 patient with paroxysmal atrial fibrillation),  $MB = 3$ ,  $R = 2-3$ ,  $FOV = 360 \times 270-297 \text{ mm}^2$ ,  $TR = 2.82-2.95 \text{ ms}$ ,  $TE = 1.45-1.47 \text{ ms}$ ,  $\text{bandwidth} = 694-992 \text{ Hz/pixel}$ , and  $\text{temporal footprint} = 169 \text{ ms to } 195 \text{ ms}$ , corresponding to phase FOV values of 75% to 82.6%. The interslice gap was 16 mm for each MB excitation, and the interslice gap was 0 between neighboring slices. For  $R = 2$  the spatial resolution was  $2.25 \text{ mm} \times 2.25 \text{ mm}$ , and for  $R = 3$  the spatial resolution was  $1.5 \text{ mm} \times 1.5 \text{ mm}$ .

All prospectively acquired MB datasets were reconstructed using both seq-SG-L+S and slice-L+S. All slices reconstructed by both methods were scored by 2 cardiologists using a 1–5 scale, with 1 corresponding to worst and 5 to best, where the assessments were based on residual artifacts, noise, sharpness of borders and overall impression. Both expert readers (C.M.K. and M.S.) have greater than 15 years of experience in cardiovascular MRI interpretation and have cardiovascular MR certification level 3. The correlation coefficient was used to assess agreement of the scores between the observers. The Wilcoxon signed rank test was used to test for differences between the reconstruction methods.

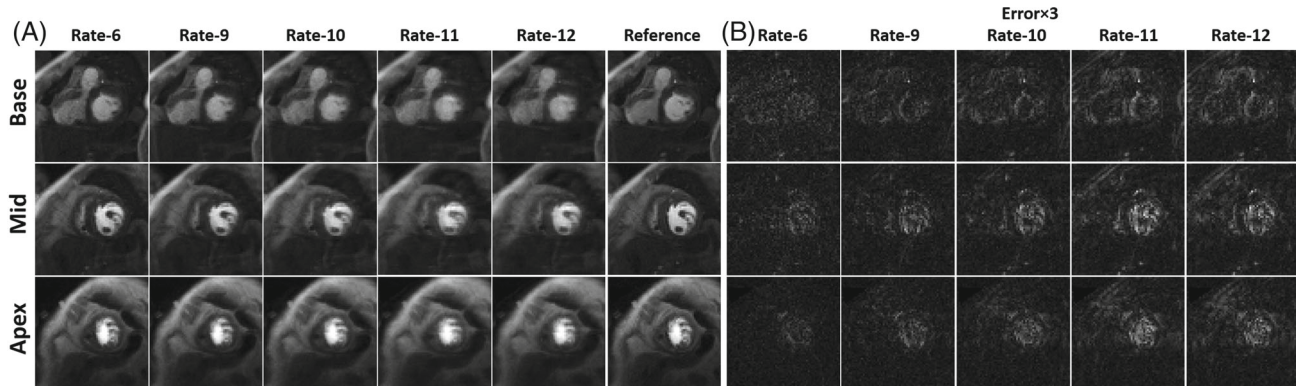
## 4 | RESULTS

### 4.1 | Evaluation of slice-L + S and comparisons with SB L + S and seq-SG-L + S using synthetic undersampled MB data

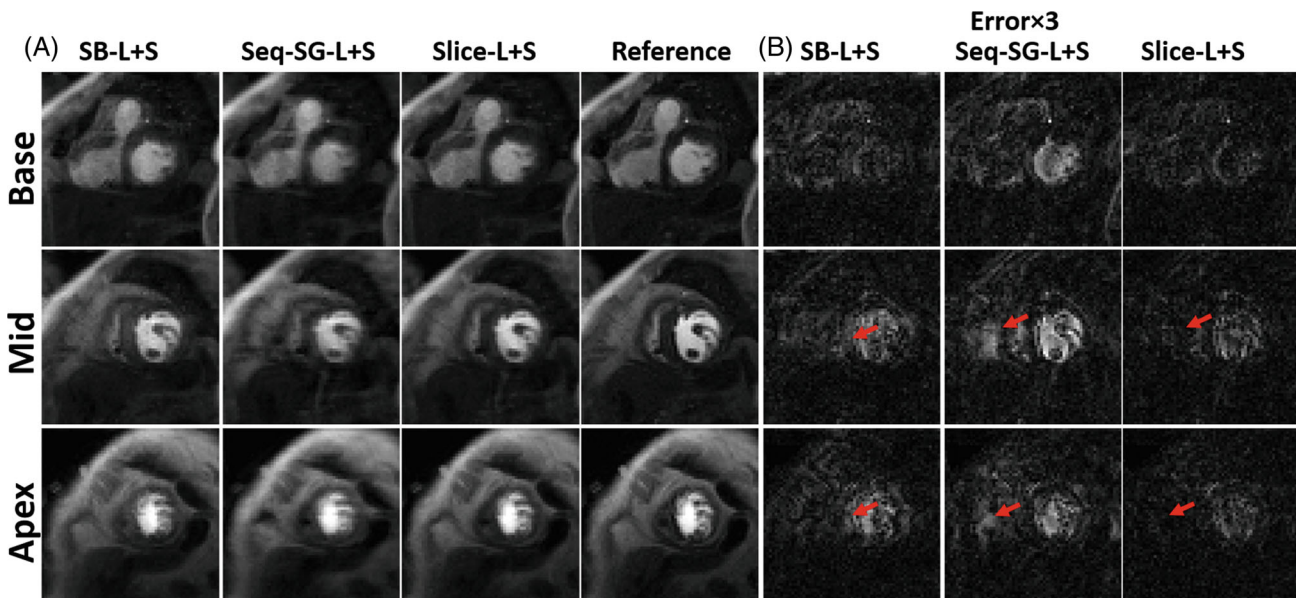
Example synthetic undersampled MB images reconstructed using slice-L+S with  $MB = 3$  and total acceleration = 6, 9, 10, 11, and 12, along with SB reference images and error maps, are shown in Figure 3A,B, respectively. As expected, residual artifacts and spatial blur increase with increasing undersampling rates. In Figure 4, example synthetic images from retrospectively undersampled data comparing SB L+S ( $R = 9$ ), seq-SG-L+S ( $MB = 3$ ,  $R = 3$ ), and slice-L+S ( $MB = 3$ ,  $R = 3$ ) are shown, along with corresponding error maps, demonstrating that slice-L+S provides the best image quality. In this example, the SB L+S method produced higher overall artifact levels compared to slice-L+S, especially at the myocardial regions highlighted by red arrows, where slice-L+S provided reduced artifacts in the myocardium and elsewhere. Slice separation artifacts are more prominent for seq-SG-L+S, and higher overall artifact levels are seen compared with slice-L+S. Examples images for 2 more cases are provided in the Supporting Information Figure S4. A limitation of results from synthetic images is that potential benefits related to a shorter acquisition window of prospective SB L+S are not accounted for.

Figure 5 summarizes the nRMSE and SSIM results for retrospectively undersampled data reconstructed using SB L+S, seq-SG-L+S, and slice-L+S for multiple total acceleration rates, and shows that slice-L+S provides the lowest nRMSE and highest SSIM for all total acceleration rates of 6–12, with SB L+S performing second best. As expected, for all reconstruction methods, nRMSE increases and SSIM decreases as the total acceleration rate increases. With comparisons over reconstruction method, nRMSE and SSIM were lower for slice-L+S compared to SB L+S and seq-SG-L+S at all acceleration rates ( $P < 0.05$ , analysis of variance). For acceleration rates of 6, 9, 10, 11, and 12, the nRMSE values for slice-L+S were  $0.023 \pm 0.004$ ,  $0.031 \pm 0.004$ ,  $0.034 \pm 0.005$ ,  $0.038 \pm 0.005$ , and  $0.042 \pm 0.006$ ; and the SSIM values were  $0.92 \pm 0.02$ ,  $0.89 \pm 0.02$ ,  $0.87 \pm 0.03$ ,  $0.86 \pm 0.03$ , and  $0.84 \pm 0.03$ , respectively. For rate 9, the nRMSE and SSIM for myocardium only are shown in Supporting Information Figures S9–S12.

Example signal x-t plots from synthetic data are shown in Figure 6 for the SB L+S, seq-SG-L+S, and slice-L+S reconstruction methods, demonstrating worse temporal fidelity for the SB-L+S and seq-SG-L+S methods and better temporal fidelity for slice-L+S compared with the reference SB x-t plots. Figure 7 quantitatively shows that



**FIGURE 3** Example images and error maps for the slice-L + S method computed using synthetic k-t undersampled MB first-pass perfusion images from a patient. Images with MB factor = 3 and  $R = 2-4$  are shown, resulting in total acceleration rates of 6–12. (A) Synthetic k-t undersampled MB data were reconstructed using the slice-L + S method. (B) Image artifacts relative to the original fully sampled reference images are shown. At MB = 3, as the undersampling factor  $R$  is increased, image artifacts and spatial blur are more prominent.  $R$ , in-plane acceleration rate.



**FIGURE 4** Comparison of the SB L + S method ( $R = 9$ ), the MB sequential operations method (seq-SG-L + S) (MB = 3 and  $R = 3$ ), and the MB slice-L + S method for reconstruction of synthetic k-t undersampled SB or MB first-pass perfusion images for 1 patient with aggregate rate 9 acceleration (A–C). Synthetic k-t undersampled SB data were reconstructed using SB L + S, and k-t undersampled MB data were reconstructed using seq-SG-L + S and slice-L + S. Image artifacts relative to the original reference SB images are shown. The SB L + S and seq-SG-L + S produced higher overall artifact levels, with slice-L + S demonstrating reductions in artifacts. In-plane residual artifacts and slice separation artifacts are more prominent for SB L + S and seq-SG-L + S, respectively, as indicated by the red arrows

slice-L + S provides higher SSIM and lower nRMSE for all the temporal measurements compared to SB L + S and seq-SG-L + S. SSIM and nRSME plots along time for 2 more cases are provided in the Supporting Information Figure S4.

All reconstructions were performed in MatLab 2019a (MathWorks) on a desktop computer (3.6 GHz Intel(R)Xeon(R) W-2123 CPU with 32 GB RAM). The computation times to reconstruct 40 measurements of 1 slice using seq-SG-L + S and slice-L + S were 460.8 and 887.9 s, respectively.

#### 4.2 | Comparison of slice-L + S and seq-SG-L + S for the reconstruction of prospectively acquired k-t undersampled MB first-pass data

Example images showing 3 slices with spatial resolution of  $1.5 \text{ mm} \times 1.5 \text{ mm}$  using MB = 3 and  $R = 3$  from 1 patient are shown in Figure 8 that compare seq-SG-L + S and slice-L + S for the reconstruction of prospectively undersampled MB first-pass data. Various time points are shown including the baseline, peak enhancement of the right



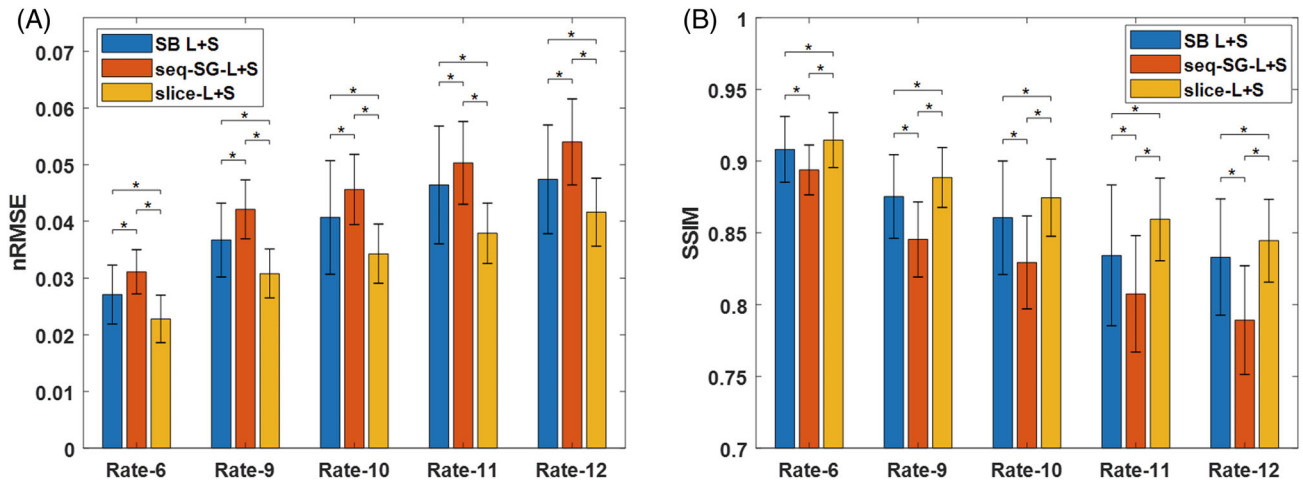


**FIGURE 5** Quantitative comparisons of different methods for reconstruction of synthetic k-t undersampled MB first-pass perfusion images for various acceleration rates. For SB L + S,  $R = 6-12$  were evaluated; and for the multiband methods,  $MB = 3$  and  $R = 2-4$  were used, leading to rate 6 to rate 12 aggregate acceleration for all methods. As shown in (A), the nRMSE was highest for the sequential operations method (seq-SG-L + S), intermediate for SB L + S, and lowest for slice-L + S ( $*P < 0.05$ , ANOVA). In (B), the SSIM was lowest for the seq-SG-L + S, intermediate for SB L + S, and highest for slice-L + S ( $*P < 0.05$ , ANOVA). Error bars indicate SDs.  $N = 7$  patients were studied. ANOVA, analysis of variance; nRMSE, normalized RMSE; SSIM, structural similarity.

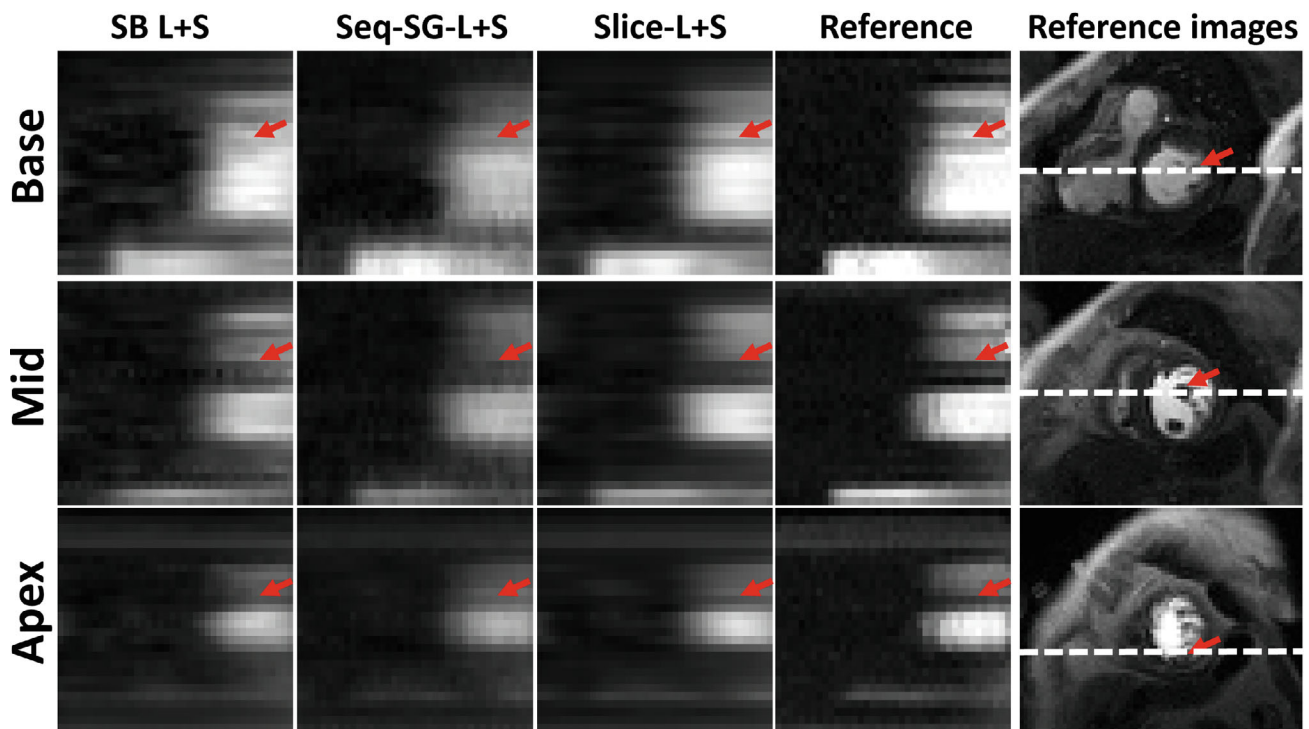


**FIGURE 6** Comparison of signal x-t plots corresponding to SB L + S ( $R = 9$ ), seq-SG-L + S ( $MB = 3$  and  $R = 3$ ), and slice-L + S ( $MB = 3$  and  $R = 3$ ) for the reconstruction of synthetic k-t undersampled perfusion images for the patient in Figure 4. Slice-L + S presents better temporal fidelity than SB L + S and seq-SG-L + S compared the fully sampled reference x-t plots

ventricular blood, peak enhancement of the left ventricular blood, and peak enhancement of the myocardium. The slice-L + S method demonstrates sharper borders and greater contrast, especially at peak myocardial

measurements. Example images, also with spatial resolution of  $1.5 \text{ mm} \times 1.5 \text{ mm}$  and  $MB = 3$  and  $R = 3$ , for an additional patient showing different time points are provided in the Supporting Information

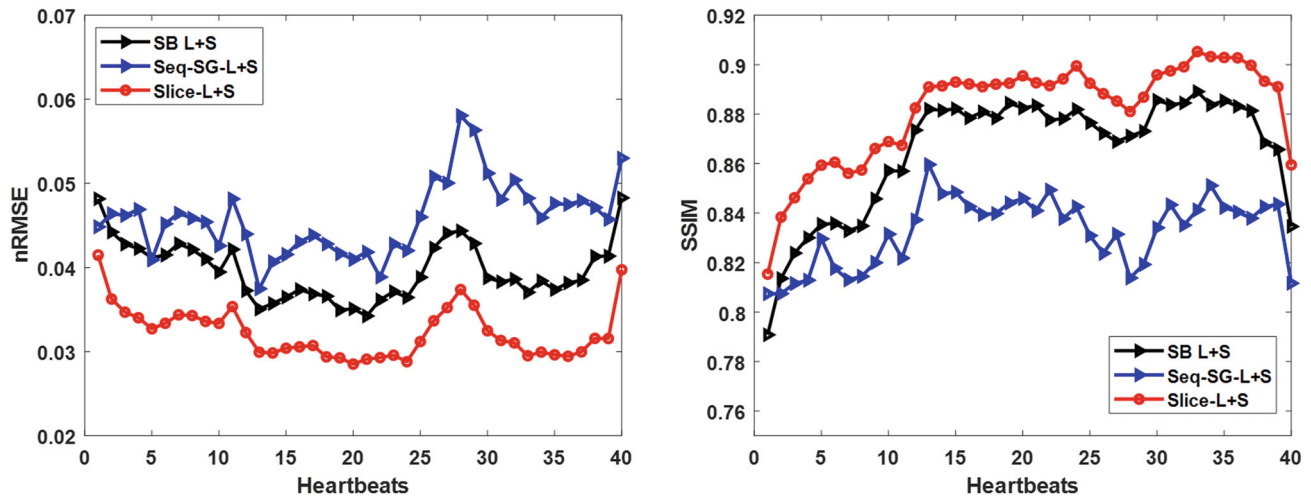


**FIGURE 7** Plots of nRMSE and SSIM along time for the 3 reconstruction methods (SB L+S, seq-SG-L+S, and slice-L+S) corresponding to synthetic k-t undersampled first-pass perfusion MRI ( $R = 9$  for the single-band method, and  $MB = 3$  and  $R = 3$  for the multiband methods) of the patient in Figure 4. The nRMSE was similar for SB L+S and seq-SG-L+S, and lower for slice-L+S for all temporal measurements. The SSIM was similar for SB L+S and seq-SG-L+S, and higher for slice-L+S for all temporal measurements

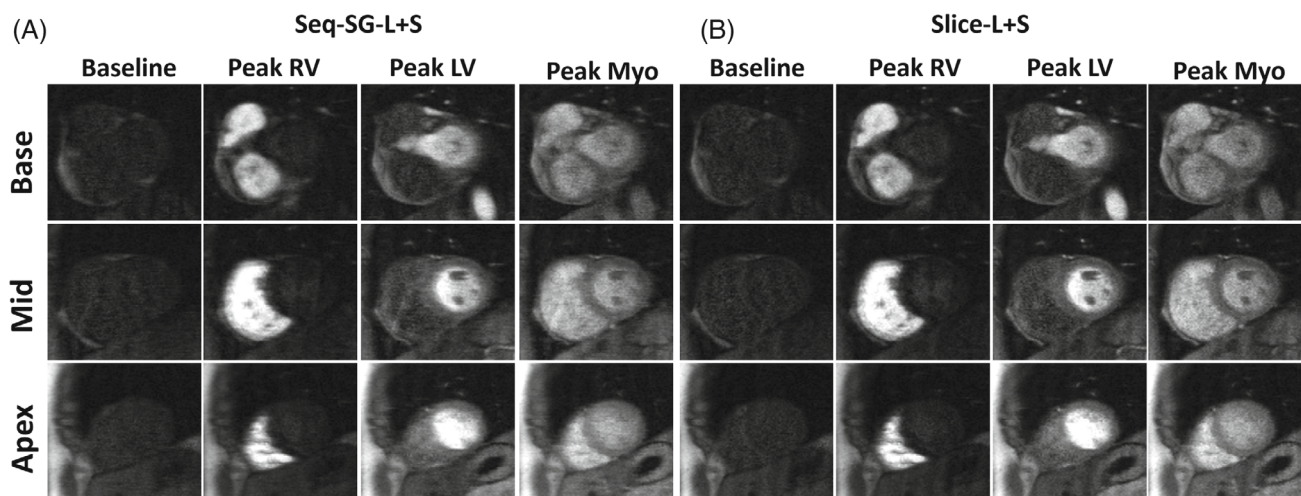


**FIGURE 8** An example comparison of (A) the sequential operations method (seq-SG-L+S) and (B) slice-L+S for the reconstruction of prospectively undersampled MB first-pass perfusion MRI ( $MB = 3$  and  $R = 3$ ) with a spatial resolution of  $1.5 \text{ mm} \times 1.5 \text{ mm}$  and 9-slice coverage of the left ventricle (3 of 9 slices are shown at different time points). Overall, seq-SG-L+S produced more artifacts, especially for peak Myo images, with slice-L+S demonstrating reductions in artifacts. The slice-L+S method provides fewer residual artifacts, sharper borders and greater contrast compared to reconstruction using sequential operations. LV, left ventricle; Myo, myocardium; RV, right ventricle.

Figure S5. Example images showing 9-slice whole-heart coverage using the 2 reconstruction methods are compared in Figure 9. Qualitatively, slice-L+S method is seen to provide fewer residual artifacts, sharper borders, and greater contrast than seq-SG-L+S. Image quality assessments by 2 experts resulted in both reviewers consistently ranking the slice-L+S method as better than the sequential method for all cases. For rate 6, the expert scoring results were  $3.3 \pm 0.87$  versus  $3.9 \pm 1.03$  ( $P < 0.05$ ) for seq-SG-L+S versus slice-L+S, respectively, with good agreement between observer

ratings ( $r = 0.54$ ,  $P < 0.05$ ). Also, expert scores were  $4.25 \pm 0.71$  and  $3.9 \pm 1.03$  for slice-L+S retrospective versus prospective studies, respectively, with good agreement between observer ratings ( $r = 0.55$ ). For rate 9, the scoring results were  $3.3 \pm 0.70$  versus  $4.0 \pm 0.63$  ( $P < 0.05$ ) for seq-SG-L+S and slice-L+S, respectively, with good agreement between observer ratings ( $r = 0.49$ ,  $P < 0.05$ ). Videos showing all first-pass measurements of 2 k-t undersampled MB datasets are provided in the Supporting Information Video S1 ( $MB = 3$  and  $R = 2$ ) and S2 ( $MB = 3$  and  $R = 3$ ).

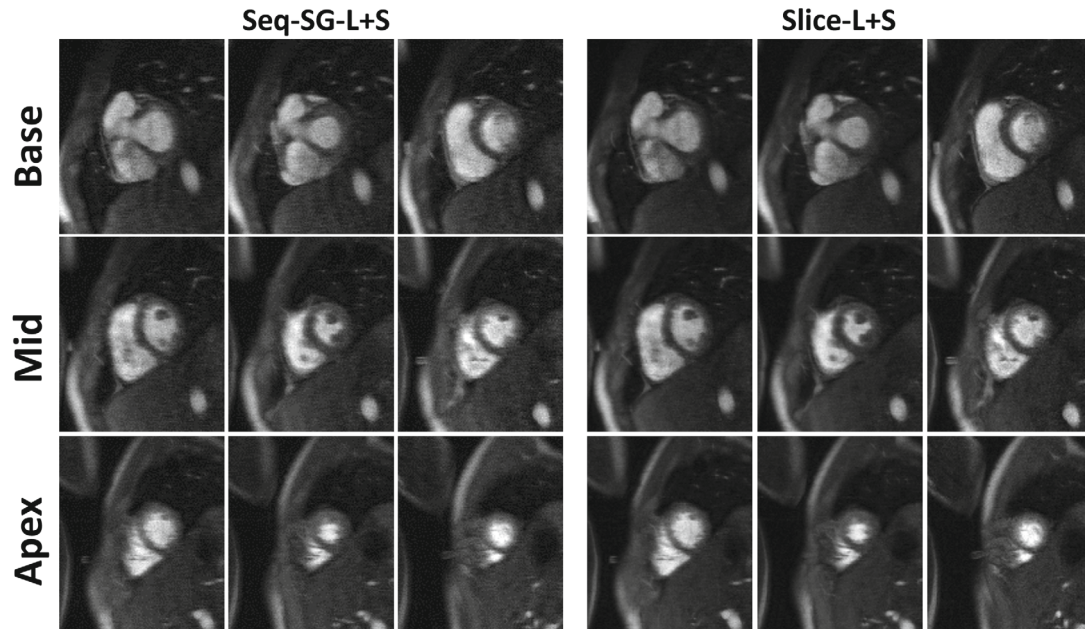


**FIGURE 9** Example images showing all 9 slices of prospectively accelerated high-resolution ( $1.5 \text{ mm} \times 1.5 \text{ mm}$ ) perfusion MRI with  $\text{MB} = 3$  and  $R = 3$  reconstructed using the sequential operations method (seq-SG-L + S) and the slice-L + S method for 1 patient. Slice-L + S shows better performance for the removal of aliasing artifacts associated with undersampling.

## 5 | DISCUSSION

We developed an iterative reconstruction method for  $k$ - $t$  undersampled MB first-pass perfusion MRI that uniquely incorporates L+S applied to coil-combined slice-separated data by using slice separation with split slice-GRAPPA when solving the MB data consistency term. It is through the use of slice-GRAPPA followed by coil combination in solving the MB data consistency term in slice-L + S that we exploit joint sparsity of coil-combined slice-separated images. The major results of our experiments are (1) slice-L + S provides a more accurate reconstruction of undersampled MB first-pass perfusion images than seq-SG-L + S; and (2) slice-L + S with a  $k$ - $t$  undersampled MB acquisition outperformed SB L + S using a  $k$ - $t$  undersampled SB acquisition (with a matched total acceleration rate) with regard to SSIM, nRMSE, and temporal fidelity. Other important aspects of this study are (1) the MB data consistency method described in Figure 2 provides a coil-combined slice-by-slice gradient that enables an efficient combination with L + S of multiple slices; (2) the MB data consistency method reduces slice separation artifacts in both  $k$ -space using split slice-GRAPPA and image space using ESPIRiT; (3) slice-L + S resolves undersampling artifacts and slice separation artifacts simultaneously; and (4) the implementation uses a variable splitting method that enabled alternation between conjugate gradient and soft thresholding in order to converge to a solution, and therefore can easily be extended to incorporate other

constraints commonly used for SB compressed sensing reconstructions.

### 5.1 | Insights into $k$ - $t$ undersampled MB reconstruction and MB data consistency terms

$k$ - $t$  undersampled MB images suffer from both coherent slice-separation artifacts and coherent and incoherent artifacts due to  $k$ - $t$  undersampling with a fully sampled  $k$ -space center and randomness at higher  $k_y$  values. Although split slice-GRAPPA provides better through-plane artifact reduction than competing noniterative methods, slice separation is imperfect.<sup>19</sup> It has been shown previously that further reduction of slice separation artifacts can be achieved using iterative methods.<sup>23,33</sup> For iterative reconstruction, the data consistency method of Equation 3 and Figure 2 can minimize the coherent artifacts related to slice separation and in-plane undersampling (as well as enforce MB data fidelity), whereas the L + S constraints of multiple slices can minimize the incoherent artifacts due to  $k$ - $t$  undersampling with randomness. The MB data consistency term in Equation 3 is different from the MB data consistency used for the slice-SPIRiT method<sup>23</sup> because slice-SPIRiT uses slice-by-slice coil information, which decreases the performance of temporal sparsity.<sup>6,34</sup> The residual artifacts of seq-SG-L + S observed in Supporting Information Videos S1 and S2 are

mainly due to the SB data consistency term. Such a SB data consistency is based on imperfectly separated data with artifacts due to slice separation and k-t undersampling. The data consistency term makes the reconstructed image consistent with corrupted SB data. In Supporting Information Appendix S1 and Supporting Information Figure S1, we investigate alternative MB data consistency terms, comparing 3 of them, all using L + S regularization. As shown in Supporting Information Figures S2 and S3, the data consistency method of slice-L + S had the best performance. The imperfect slice-separating kernel affects all methods, including slice-L + S. We found that the use of both of a slice-separating kernel and ESPiRiT improves performance.

## 5.2 | Solving slice-L + S using variable splitting

Because the slice-L + S optimization function includes an  $l_2$  norm, nuclear norm, and  $l_1$  norm, we used variable splitting to decompose the global nonlinear minimization into 2 subproblems. Our algorithm alternated between the 2 subproblems, where the data consistency subproblem was solved using the LSQR conjugate gradient method and the L + S subproblem was solved using iterative soft thresholding, and this approach provided an efficient and stable method to solve Equation 3. Instead of enforcing the low-rank constraint for each slice,<sup>35</sup> slice-L + S applies the temporal low-rank plus sparse constraint to multiple concatenated slices, which leverages multiple slices to generate a bigger matrix, providing better low-rank characteristics.<sup>36</sup>

## 5.3 | Comparison with SB L + S

We compared slice-L + S, seq-SG-L + S, and SB L + S using synthetic datasets with the same total accelerations of 6–12. When the same total acceleration rates are used for SB and MB imaging, seq-SG-L + S did not outperform SB L + S, which indicates that k-t undersampled MB imaging may not always outperform k-t undersampled SB imaging, and a well-designed reconstruction method for k-t undersampled MB imaging is needed. Also, we observed in Figure 5 that the SDs of the nRMSE and SSIM values for SB L + S are higher than slice-L + S and seq-SG-L + S for acceleration rates of 6–12. The k-t undersampling rate of SB imaging is MB times higher than that of MB imaging. The higher SD may be due to higher k-t undersampling rates for SB imaging and lower SNR of k-t undersampled SB imaging with the same total acceleration rates. We also note that the lower undersampling rate for MB imaging

results in a longer acquisition window, which could be a disadvantage, especially during adenosine stress imaging, and that our study did not account for potential benefits to SB L + S related to a shorter acquisition window.

## 5.4 | Comparison with other k-t MB reconstruction models

In conventional undersampled MB imaging, split slice-GRAPPA followed by GRAPPA<sup>37</sup> has been previously used,<sup>18,19</sup> and split slice-GRAPPA has been shown to be an effective method for MB cardiac MRI.<sup>23,38,39</sup> These results motivated the selection of split slice-GRAPPA for slice separation within seq-SG-L + S and slice-L + S. In addition to the methods employed in the present study, other methods to reconstruct k-t undersampled MB imaging have been proposed, one of which is simultaneous multi-slice (SMS)-Slice-L1-SPIRiT.<sup>40</sup> In comparing slice-L + S with SMS-Slice-L1-SPIRiT, we note that whereas slice-L + S (a) exploits slice-separated joint sparsity, (b) uses L + S regularization of multiple slices, and (c) utilizes slice-GRAPPA to perform slice separation (facilitating slice-separated joint sparsity), SMS-Slice-L1-SPIRiT does not exploit joint sparsity, enforces S, and utilizes slice-GRAPPA for coil consistency but not for slice separation. Also, coil-by-coil compressed sensing, as performed in SMS-Slice-L1-SPIRiT, increases the memory requirement and reconstruction time.<sup>8,10,40</sup> Other methods, such as SMS- low-rank modeling of local k-space neighborhoods, have also been proposed for calibrationless single- or multicoil MB reconstruction, although temporal L + S and through-plane coil information were not included. Recently, an SMS-balance steady state free precession compressed sensing method was proposed with spatial and temporal wavelet regularizations<sup>12</sup>; however, it did not use through-plane coil information in the MB data consistency term. Another method, readout concatenated k-space-SPIRiT, based on readout concatenation and coil self-consistency, has not been combined with joint sparsity.<sup>41</sup>

## 5.5 | Limitations and future work

We evaluated slice-L + S using Cartesian first-pass perfusion MRI because Cartesian is the most widely used trajectory; however, the method could be modified and applied to non-Cartesian trajectories. We investigated MB = 3 and R = 2–4 using synthetic datasets and MB = 3 and R = 2 and 3 using prospectively acquired MB datasets, but other combinations of through-plane and in-plane acceleration factors should be compared in the future. Although a proof

of concept was shown using retrospective studies, future studies could compare k-t undersampled SB and MB L + S methods with matched total acceleration rates to further demonstrate the advantages of slice-L + S for first-pass perfusion MRI. We quantified residual artifacts, including artifacts due to slice-leakage and k-t undersampling, by error maps relative to SB reference images, similar to the approach used by Ref.<sup>19</sup> We acknowledge that these methods do not distinguish between artifacts due to k-t undersampling versus artifacts due to slice leakage. We tested our method in subjects undergoing MRI at rest; future studies could evaluate slice-L + S for stress imaging. We tuned the model hyperparameters using retrospective data, which, due to differences in eddy currents and object motion in data sampling windows of different durations, is not identical to prospectively acquired data. However, cardiologist scoring showed that prospective and retrospective data reconstructed using slice-L + S provided similar image quality scores and that image quality was considered diagnostic. These results suggest that the choices of slice-L + S hyperparameters are reasonable for prospectively acquired undersampled MB data. The computation time of slice-L + S may be too long for online reconstruction. Faster computation could be achieved using deep learning. The number of datasets used to evaluate our methods was limited, and further experience with more subjects would be warranted to move these methods toward clinical use.

We utilized the proposed MB data consistency method to develop slice-L + S. However, our MB data consistency could be used with other regularizations such as wavelets<sup>42</sup> to reconstruct nondynamic images using soft-thresholding algorithms like  $l_1$ -ESPIRiT.<sup>29</sup> To incorporate the low-rank constraint, we applied the low-rank plus sparse constraint to concatenated multiple slices; however, the subspace method<sup>43,44</sup> could also be utilized with the proposed MB data consistency. Other types of MB reconstructions should also be compared in the future such as regularized nonlinear inversion.<sup>24</sup>

## 6 | CONCLUSION


A method to reconstruct k-t undersampled MB first-pass perfusion images was developed that outperforms approaches that use the sequential operations of slice separation followed by L + S and SB L + S with the same total acceleration rates. The MB data consistency method provides a coil-combined slice-by-slice gradient to efficiently reduce artifacts due to slice separation and k-t undersampling. With slice-L + S and k-t undersampled MB imaging, 9 slices may be acquired per heartbeat,

providing improved coverage and 1.5 mm × 1.5 mm spatial resolution for first-pass perfusion MRI.

## CONFLICT OF INTEREST

Frederick H. Epstein, Michael Salerno and Kenneth C. Bilchick have research support from Siemens Healthineers.

## ORCID

Changyu Sun  <https://orcid.org/0000-0001-8102-7130>

Daniel Weller  <https://orcid.org/0000-0001-9818-7325>

## REFERENCES

- Gerber BL, Raman SV, Nayak K, et al. Myocardial first-pass perfusion cardiovascular magnetic resonance: history, theory, and current state of the art. *J Cardiovasc Magn Reson* 2008;10:18.
- Kellman P, Arai AE. Imaging sequences for first pass perfusion – a review. *J Cardiovasc Magn Reson*. 2007;9:525-537.
- Kramer CM, Barkhausen J, Flamm SD, Kim RJ, Nagel E. Society for Cardiovascular Magnetic Resonance Board of trustees task force on standardized P. standardized cardiovascular magnetic resonance (CMR) protocols 2013 update. *J Cardiovasc Magn Reson*. 2013;15:91.
- Motwani M, Jogiya R, Kozerke S, Greenwood JP, Plein S. Advanced cardiovascular magnetic resonance myocardial perfusion imaging: high-spatial resolution versus 3-dimensional whole-heart coverage. *Circ Cardiovasc Imaging*. 2013;6:339-348.
- Adluru G, Awate SP, Tasdizen T, Whitaker RT, Dibella EV. Temporally constrained reconstruction of dynamic cardiac perfusion MRI. *Magn Reson Med*. 2007;57:1027-1036.
- Otazo R, Kim D, Axel L, Sodickson DK. Combination of compressed sensing and parallel imaging for highly accelerated first-pass cardiac perfusion MRI. *Magn Reson Med*. 2010;64:767-776.
- Otazo R, Candes E, Sodickson DK. Low-rank plus sparse matrix decomposition for accelerated dynamic MRI with separation of background and dynamic components. *Magn Reson Med*. 2015;73:1125-1136.
- Stab D, Wech T, Breuer FA, et al. High resolution myocardial first-pass perfusion imaging with extended anatomic coverage. *J Magn Reson Imaging* 2014;39:1575-1587.
- Nazir MS, Neji R, Speier P, et al. Simultaneous multi slice (SMS) balanced steady state free precession first-pass myocardial perfusion cardiovascular magnetic resonance with iterative reconstruction at 1.5 T. *J Cardiovasc Magn Reson* 2018;20:84.
- Yang Y, Meyer CH, Epstein FH, Kramer CM, Salerno M. Whole-heart spiral simultaneous multi-slice first-pass myocardial perfusion imaging. *Magn Reson Med*. 2019;81:852-862.
- Tian Y, Mendes J, Pedgaonkar A, et al. Feasibility of multiple-view myocardial perfusion MRI using radial simultaneous multi-slice acquisitions. *PLoS One* 2019;14:e0211738.
- McElroy S, Ferrazzi G, Nazir MS, et al. Combined simultaneous multislice bSSFP and compressed sensing for first-pass myocardial perfusion at 1.5 T with high spatial resolution and coverage. *Magn Reson Med* 2020;84:3103-3116.

13. Kellman P, Epstein FH, McVeigh ER. Adaptive sensitivity encoding incorporating temporal filtering (TSENSE). *Magn Reson Med*. 2001;45:846-852.
14. Breuer FA, Kellman P, Griswold MA, Jakob PM. Dynamic autocalibrated parallel imaging using temporal GRAPPA (TGRAPPA). *Magn Reson Med*. 2005;53:981-985.
15. Chen X, Salerno M, Yang Y, Epstein FH. Motion-compensated compressed sensing for dynamic contrast-enhanced MRI using regional spatiotemporal sparsity and region tracking: block low-rank sparsity with motion-guidance (BLOSM). *Magn Reson Med*. 2014;72:1028-1038.
16. Lingala SG, Hu Y, DiBella E, Jacob M. Accelerated dynamic MRI exploiting sparsity and low-rank structure: k-t SLR. *IEEE Trans Med Imaging*. 2011;30:1042-1054.
17. Blaimer M, Breuer FA, Seiberlich N, et al. Accelerated volumetric MRI with a SENSE/GRAPPA combination. *J Magn Reson Imaging* 2006;24:444-450.
18. Setsompop K, Gagoski BA, Polimeni JR, Witzel T, Wedeen VJ, Wald LL. Blipped-controlled aliasing in parallel imaging for simultaneous multislice echo planar imaging with reduced g-factor penalty. *Magn Reson Med*. 2012;67:1210-1224.
19. Cauley SF, Polimeni JR, Bhat H, Wald LL, Setsompop K. Interslice leakage artifact reduction technique for simultaneous multislice acquisitions. *Magn Reson Med*. 2014;72:93-102.
20. Zhu K, Dougherty RF, Wu H, et al. Hybrid-space SENSE reconstruction for simultaneous multi-slice MRI. *IEEE Trans Med Imaging* 2016;35:1824-1836.
21. Breuer FA, Blaimer M, Heidemann RM, Mueller MF, Griswold MA, Jakob PM. Controlled aliasing in parallel imaging results in higher acceleration (CAIPIRINHA) for multi-slice imaging. *Magn Reson Med*. 2005;53:684-691.
22. Yutzy SR, Seiberlich N, Duerk JL, Griswold MA. Improvements in multislice parallel imaging using radial CAIPIRINHA. *Magn Reson Med*. 2011;65:1630-1637.
23. Sun C, Yang Y, Cai X, et al. Non-Cartesian slice-GRAPPA and slice-SPIRiT reconstruction methods for multiband spiral cardiac MRI. *Magn Reson Med* 2020;83:1235-1249.
24. Rosenzweig S, Holme HCM, Wilke RN, Voit D, Frahm J, Uecker M. Simultaneous multi-slice MRI using cartesian and radial FLASH and regularized nonlinear inversion: SMS-NLINV. *Magn Reson Med*. 2018;79:2057-2066.
25. Weingartner S, Moeller S, Schmitter S, et al. Simultaneous multislice imaging for native myocardial T1 mapping: improved spatial coverage in a single breath-hold. *Magn Reson Med* 2017;78:462-471.
26. Huang F, Chen Y, Yin W, et al. A rapid and robust numerical algorithm for sensitivity encoding with sparsity constraints: self-feeding sparse SENSE. *Magn Reson Med* 2010;64:1078-1088.
27. Barth M, Breuer F, Koopmans PJ, Norris DG, Poser BA. Simultaneous multislice (SMS) imaging techniques. *Magn Reson Med*. 2016;75:63-81.
28. Deshmane A, Gulani V, Griswold MA, Seiberlich N. Parallel MR imaging. *J Magn Reson Imaging*. 2012;36:55-72.
29. Uecker M, Lai P, Murphy MJ, et al. ESPIRiT – an eigenvalue approach to autocalibrating parallel MRI: where SENSE meets GRAPPA. *Magn Reson Med* 2014;71:990-1001.
30. Lustig M, Pauly JM. SPIRiT: iterative self-consistent parallel imaging reconstruction from arbitrary k-space. *Magn Reson Med*. 2010;64:457-471.
31. Wang Z, Bovik AC, Sheikh HR, Simoncelli EP. Image quality assessment: from error visibility to structural similarity. *IEEE Trans Image Process*. 2004;13:600-612.
32. Zhang T, Pauly JM, Vasanawala SS, Lustig M. Coil compression for accelerated imaging with Cartesian sampling. *Magn Reson Med*. 2013;69:571-582.
33. Demirel OB, Weingärtner S, Moeller S, Akçakaya M. Multi-Band SPIRiT Strategies for Improved Simultaneous Multi-slice Myocardial T1 Mapping. Proceedings of the 27th Annual meeting of ISMRM, Montréal, Québec, Canada, 2019. p. 2126.
34. Murphy M, Alley M, Demmel J, Keutzer K, Vasanawala S, Lustig M. Fast l(1)-SPIRiT compressed sensing parallel imaging MRI: scalable parallel implementation and clinically feasible runtime. *IEEE Trans Med Imaging*. 2012;31:1250-1262.
35. Hamilton JI, Jiang Y, Ma D, et al. Simultaneous multislice cardiac magnetic resonance fingerprinting using low rank reconstruction. *NMR Biomed* 2019;32:e4041.
36. Haldar JP, Zhuo JW. P-LORAKS: low-rank modeling of local k-space neighborhoods with parallel imaging data. *Magn Reson Med*. 2016;75:1499-1514.
37. Griswold MA, Jakob PM, Heidemann RM, et al. Generalized autocalibrating partially parallel acquisitions (GRAPPA). *Magn Reson Med* 2002;47:1202-1210.
38. Schmitter S, Moeller S, Wu X, et al. Simultaneous multislice imaging in dynamic cardiac MRI at 7T using parallel transmission. *Magn Reson Med* 2017;77:1010-1020.
39. Rapacchi S, Troalen T, Bentatou Z, et al. Simultaneous multi-slice cardiac cine with Fourier-encoded self-calibration at 7 Tesla. *Magn Reson Med* 2019;81:2576-2587.
40. Wang JY, Yang Y, Weller DS, et al. High spatial resolution spiral first-pass myocardial perfusion imaging with whole-heart coverage at 3 T. *Magn Reson Med* 2021;86:648-662.
41. Demirel OB, Weingartner S, Moeller S, Akçakaya M. Improved simultaneous multislice cardiac MRI using readout concatenated k-space SPIRiT (ROCK-SPIRiT). *Magn Reson Med*. 2021;85:3036-3048.
42. Lustig M, Donoho D, Pauly JM. Sparse MRI: the application of compressed sensing for rapid MR imaging. *Magn Reson Med*. 2007;58:1182-1195.
43. Feng L, Wen Q, Huang C, Tong A, Liu F, Chandarana H. GRASP-pro: improving GRASP DCE-MRI through self-calibrating subspace-modeling and contrast phase automation. *Magn Reson Med*. 2020;83:94-108.
44. Zhao B, Bilgic B, Adalsteinsson E, Griswold MA, Wald LL, Setsompop K. Simultaneous multislice magnetic resonance fingerprinting with low-rank and subspace modeling. 2017 39th Annual International Conference of the IEEE Engineering in Medicine and Biology Society (EMBC) 2017: 3264-3268.

## SUPPORTING INFORMATION

Additional supporting information may be found in the online version of the article at the publisher's website.

**Appendix S1.** Comparison of two alternative MB data consistency methods with the L+S constraint with the proposed slice-L+S method

**Appendix S2.** Information describing twenty-one patients undergoing clinically-ordered first-pass perfusion studies.

**Figure S1.** Schematic of alternative MB data consistency methods using (A) in-plane sensitivity maps only ( $\lambda_2 = 0$ ) and (B) in-plane sensitivity maps and consistency with MB data that has been separated using a split slice-GRAPPA kernel as an additional  $l_2$  constraint ( $\lambda_2 > 0$ )

**Figure S2.** Slice-L+S, as proposed, was compared to slice-L+S implemented using two alternative MB data consistency methods (ADCM<sub>1</sub> and ADCM<sub>2</sub>) of Equation S1 and Figure S1 using synthetic undersampled MB first-pass perfusion MRI (MB = 3 and R = 2)

**Figure S3.** Quantitative analyses of the comparisons of different MB data consistency methods using synthetic k-t undersampled MB first-pass perfusion MRI (MB = 3 and R = 2) of 3 patients

**Figure S4.** Comparison of the SB L+S method (R = 9), the sequential operations method (seq-SG-L+S) (MB = 3 and R = 3), and slice-L+S (MB = 3 and R = 3) for reconstruction of synthetic k-t undersampled MB first-pass perfusion MRI with the same total acceleration rate of 9 for two patients (A and B)

**Figure S5.** Comparison of (A) the sequential operations method (seq-SG-L+S) and (B) the slice-L+S method for reconstruction of prospectively k-t undersampled MB first-pass perfusion images (MB = 3 and R = 3) with a spatial resolution of 1.5 mm × 1.5 mm and coverage of nine slices (3 slices are shown) at different time points

**Figure S6.** (A) Mean SSIM and nRMSE of all temporal measurements for one patient using different combinations of the weighting parameters for L and S using SB images as references. The results indicate that 0.01 for  $\lambda_L$  and  $0.01 \times M_0$  for  $\lambda_S$  are the optimal weighting parameters for the proposed slice-L+S method. (B) Plot of residual norm (in log scale) versus number of iterations for the slice-L+S reconstruction.

**Figure S7.** Mean SSIM and nRMSE of all temporal measurements for one patient using different combinations of the weighting parameters for L and S using SB images as references. The results indicate that 0.014 for  $\lambda_L$  and  $0.018 \times M_0$  for  $\lambda_S$  are the optimal weighting parameters for the SB L+S method at 1.5 T scanner

**Figure S8.** Mean SSIM and nRMSE of all temporal measurements for one patient using different combinations of the weighting parameters for L and S using SB images as references. The results indicate that 0.018 for  $\lambda_L$  and  $0.026 \times M_0$  for  $\lambda_S$  are the optimal weighting parameters for the seq-SG-L+S method at 1.5 T scanner

**Figure S9.** Quantitative comparisons of different methods for reconstruction of synthetic k-t undersampled MB

first-pass perfusion images using rate-9 acceleration, considering just the myocardial region of interest at different slice locations. As shown in (A), the nRMSE was highest for SB L+S, intermediate for seq-SG-L+S, and lowest for slice-L+S ( $*p < 0.05$ , ANOVA). In (B), the SSIM was lowest for SB L+S, intermediate for seq-SG-L+S, and highest for slice-L+S ( $*p < 0.05$ , ANOVA). Error bars indicate standard deviations. N = 7 patients were studied

**Figure S10.** Quantitative comparisons of different methods for reconstruction of synthetic k-t undersampled MB first-pass perfusion images using rate-9 acceleration, considering just the American Heart Association segments of the basal slice as the regions of interest. As shown in (A), the nRMSE was highest for SB L+S, intermediate for seq-SG-L+S, and lowest for slice-L+S ( $*p < 0.05$ , ANOVA). In (B), the SSIM was lowest for SB L+S, intermediate for seq-SG-L+S, and highest for slice-L+S ( $*p < 0.05$ , ANOVA). Error bars indicate standard deviations. N = 7 patients were studied

**Figure S11.** Quantitative comparisons of different methods for reconstruction of synthetic k-t undersampled MB first-pass perfusion images using rate-9 acceleration, considering just the American Heart Association segments of the midventricular slice as the regions of interest. As shown in (A), the nRMSE was highest for SB L+S, intermediate for seq-SG-L+S, and lowest for slice-L+S ( $*p < 0.05$ , ANOVA). In (B), the SSIM was lowest for SB L+S, intermediate for seq-SG-L+S, and highest for slice-L+S ( $*p < 0.05$ , ANOVA). Error bars indicate standard deviations. N = 7 patients were studied

**Figure S12.** Quantitative comparisons of different methods for reconstruction of synthetic k-t undersampled MB first-pass perfusion images using rate-9 acceleration, considering just the American Heart Association segments of the apical slice as the regions of interest. As shown in (A), the nRMSE was highest for SB L+S, intermediate for seq-SG-L+S, and lowest for slice-L+S ( $*p < 0.05$ , ANOVA). In (B), the SSIM was lowest for SB L+S, intermediate for seq-SG-L+S, and highest for slice-L+S ( $*p < 0.05$ , ANOVA). Error bars indicate standard deviations. N = 7 patients were studied

**Video S1.** Comparison of (Left) the sequential operations method (seq-SG-L+S) and (Right) the slice-L+S method for reconstruction of prospectively k-t undersampled MB first-pass perfusion images (MB = 3 and R = 2) with a spatial resolution of 2.25 mm × 2.25 mm and coverage of nine slices at forty time points. Overall, the slice-L+S method provides sharper borders and fewer artifacts compared to seq-SG-L+S

**Video S2.** Comparison of (Left) the sequential operations method (seq-SG-L + S) and (Right) the slice-L + S method for reconstruction of prospectively k-t undersampled MB first-pass perfusion images ( $MB = 3$  and  $R = 3$ ) with a spatial resolution of  $1.5 \text{ mm} \times 1.5 \text{ mm}$  and coverage of nine slices at forty time points. Overall, the slice-L + S method provides sharper borders and fewer artifacts compared to seq-SG-L + S

**How to cite this article:** Sun C, Robinson A, Wang Y, et al. A Slice-Low-Rank Plus Sparse (slice-L + S) Reconstruction Method for k-t Undersampled Multiband First-Pass Myocardial Perfusion MRI. *Magn Reson Med*. 2022;88:1140-1155. doi: 10.1002/mrm.29281